



# Particle Nanosizing and Coating with an Ionic Liquid: Two Routes to Improve the Transport Properties of $\text{Na}_3\text{V}_2(\text{PO}_4)_2\text{F}_2$ .

Jacob Olchowka, Runhe Fang, Rafael Bianchini Nuernberg, Chloé Pablos,  
Dany Carlier, Sophie Cassaignon, Laurence Croguennec

## ► To cite this version:

Jacob Olchowka, Runhe Fang, Rafael Bianchini Nuernberg, Chloé Pablos, Dany Carlier, et al.. Particle Nanosizing and Coating with an Ionic Liquid: Two Routes to Improve the Transport Properties of  $\text{Na}_3\text{V}_2(\text{PO}_4)_2\text{F}_2$ .. Nanoscale, 2022, 14 (24), pp.8663-8676. 10.1039/d2nr01080a . hal-03692962

**HAL Id: hal-03692962**

**<https://u-picardie.hal.science/hal-03692962>**

Submitted on 22 Jun 2022

**HAL** is a multi-disciplinary open access archive for the deposit and dissemination of scientific research documents, whether they are published or not. The documents may come from teaching and research institutions in France or abroad, or from public or private research centers.

L'archive ouverte pluridisciplinaire **HAL**, est destinée au dépôt et à la diffusion de documents scientifiques de niveau recherche, publiés ou non, émanant des établissements d'enseignement et de recherche français ou étrangers, des laboratoires publics ou privés.

# Particles' nanosizing and coating by an ionic liquid: two routes to improve transport properties of $\text{Na}_3\text{V}_2(\text{PO}_4)_2\text{FO}_2$

Jacob Olchowka<sup>a,d,e,\*</sup>, Runhe Fang<sup>b,d</sup>, Rafael Bianchini Nuernberg<sup>a</sup>, Chloé Pablos<sup>a,c,d</sup>, Dany Carlier<sup>a,d,e</sup>, Sophie Cassaignon<sup>b,d,\*</sup>, Laurence Croguennec<sup>a,d,e</sup>

<sup>a</sup> Univ. Bordeaux, CNRS, Bordeaux INP, ICMCB, UMR 5026, F-33600 Pessac, France

<sup>b</sup> Sorbonne Université, CNRS, Laboratoire Chimie de la Matière Condensée de Paris, LCMCP, UMR 7574, 4 Place Jussieu, 75005 Paris, France

<sup>c</sup> Laboratoire de Réactivité et de Chimie des Solides, Université de Picardie Jules Verne, CNRS-UMR 7314, F-80039 Amiens Cedex 1, France

<sup>d</sup> RS2E, Réseau Français sur le Stockage Electrochimique de l'Energie, CNRS 3459, 80039 Amiens Cedex 1, France.

<sup>e</sup> ALISTORE-ERI European Research Institute, CNRS 3104, 80039 Amiens Cedex 1, France

**Abstract:**  $\text{Na}_3\text{V}_2(\text{PO}_4)_2\text{FO}_2$  is a serious candidate for a practical use as positive electrode material in Na-ion batteries thanks to its high voltage and excellent structural stability upon cycling. However, its limited intrinsic transport properties limit its performance at fast charge/discharge rates. In this work, two efficient approaches are presented to optimize the electrical conductivity of the electrode material: particles' nanosizing and particles' coating by an ionic liquid (IL). The former reveals that particle's downsizing from micrometer to nanometer range improves the electronic conductivity by more than two orders of magnitude, which greatly improves the rate capability without affecting the capacity retention. On the other hand, the original surface modification by applying an IL coating strongly enhances the ionic mobility and offers new perspectives to improve the energy storage performance by designing the electrode materials' surface composition.

## 1. Introduction

Human-induced climate problem is already impacting the weather and producing extreme climate in every inhabited region across the world such as the frequent heatwaves, heavy precipitation, droughts and tropical cyclones.<sup>1</sup> To face this problem, the main solution is based on limiting the cumulative CO<sub>2</sub> and other greenhouse gas emissions. To do so, one of the major methods is to convert the fossil fuels-based power station, led by coal-fired power plants, to alternative energy like solar and wind energy accompanied with performant energy storage systems, which can store the additional power during peak production periods and supply it to the grid during low hours to reduce burden on the electric grid. Complementary to the wide spread lithium ion battery, sodium ion battery is an environmentally friendly and reliable choice for large-scale energy storage.<sup>2-5</sup> Among the various families of positive electrode materials, despite weight penalty versus layered oxides, polyanionic ones attract much attention thank to their high average operating potential and structural stability. The most studied and promising are the NASICON Na<sub>3</sub>V<sub>2</sub>(PO<sub>4</sub>)<sub>3</sub>,<sup>6,7</sup> Na<sub>4</sub>MnV(PO<sub>4</sub>)<sub>3</sub>,<sup>8,9</sup> Na<sub>4</sub>FeV(PO<sub>4</sub>)<sub>3</sub><sup>10,11</sup> and the vanadium phosphate oxyfluoride series Na<sub>3</sub>V<sup>3+</sup><sub>2-y</sub>V<sup>4+</sup><sub>y</sub>(PO<sub>4</sub>)<sub>2</sub>F<sub>3-y</sub>O<sub>y</sub> (NVPFO<sub>y</sub>).<sup>12,13</sup> Dealing with this latter, Na<sub>3</sub>V<sup>4+</sup><sub>2</sub>(PO<sub>4</sub>)<sub>2</sub>FO<sub>2</sub>, the most oxidized member of NVPFO<sub>y</sub> family, exhibits a slightly lower average working potential compared to Na<sub>3</sub>V<sup>3+</sup><sub>2</sub>(PO<sub>4</sub>)<sub>2</sub>F<sub>3</sub> (~ 3.8 V vs Na/Na<sup>+</sup> for NVPFO<sub>2</sub> versus ~ 3.95 V vs Na/Na<sup>+</sup> for NVPF for a similar capacity).<sup>12,14</sup> However, the oxygen for fluorine substitution enhances the Na<sup>+</sup> mobility and stabilizes the structure at overcharged states, making NVPFO<sub>2</sub> and mixed anionic NVPFO<sub>y</sub> still of interest for practical purposes.<sup>12,15</sup>

Na<sub>3</sub>V<sup>3+</sup><sub>2-y</sub>V<sup>4+</sup><sub>y</sub>(PO<sub>4</sub>)<sub>2</sub>F<sub>3-y</sub>O<sub>y</sub> is composed of V<sub>2</sub>O<sub>8+y</sub>F<sub>3-y</sub> bi-octahedral units, which are connected by PO<sub>4</sub> groups to generate a three-dimensional structure. Although, the robust framework supported by the PO<sub>4</sub><sup>3-</sup> groups leads to stable long cycling capability, the isolated transition metals in this structure result in rather low intrinsic electronic conductivity.<sup>16</sup> Additionally, Notten et al. recently demonstrates that the poor rate performance of NVPF is related to the low Na<sup>+</sup> diffusion coefficient in the material.<sup>17</sup> The authors have shown that hard carbon diffusion coefficient is one order of magnitude higher than that of the polyanionic material. Thus, the NVPFO<sub>y</sub> family of material suffers from significant capacity loss at high charging/discharging rates. In recent years, plenty of methods were proposed to tackle this problem, such as the application of a carbon coating or the formation of composites with carbons (carbon nanotube, reduced graphene oxide or amorphous carbon),<sup>18-21</sup> partial

transition metal substitution (Al, Cr, Mn, Y, Zr, Ga...) <sup>22–28</sup> and morphology design (flower, sand rose, nano/micro-sphere, nano/micro-cube ...) <sup>29–34</sup> etc. Among the various synthesis methods, the morphology control and the hybridation with a carbon-based conductive phase are often carried out by hydrothermal/solvothermal synthesis. <sup>34,35</sup> However, this synthesis process leads most often to partial oxidation of vanadium and to a  $V^{3+}/V^{4+}$  ratio difficult to be controlled in the final composition, which drastically affects the energy storage performance and make thus difficult to evaluate the sole influence of morphology. <sup>34,36–39</sup> Recently Olchowka et al. reported an original ionothermal synthesis leading to NVPFO<sub>2</sub> particles coated by ionic liquid (IL) EMI TFSI. <sup>40</sup> Their energy storage performance appear promising, even if the effect of IL coating is not fully understood yet. <sup>40</sup>

In this work, Na<sub>3</sub>V<sub>2</sub>(PO<sub>4</sub>)<sub>2</sub>FO<sub>2</sub> was synthesized through three different methods (solid state reaction, ionothermal and solvothermal syntheses) to investigate the effect on the electrical properties of particles' downsizing and formation of an ionic liquid coating. For each compound, the final V<sup>4+</sup> oxidation state as well as the composition were meticulously confirmed combining X-ray diffraction and different spectroscopies. The influence of particles' size and IL coating on electronic and ionic conductivities was investigated through electrochemical impedance spectroscopy, whereas electrochemical tests allowed to evaluate the impact on the energy storage performance.

## 2. Experimental Section

### 2.1 Materials preparation

NVPFO<sub>2</sub> materials were synthesized through three different methods. NVPFO<sub>2</sub>-Iono was obtained by ionothermal synthesis.  $\alpha$ -VOPO<sub>4</sub>·2H<sub>2</sub>O (homemade) and NaF (molar ratio of 2/3) were placed in Teflon Parr autoclave with 6 mL of EMI-TFSI (1-ethyl-3-methyl-imidazolium bis(trifluoromethylsulfonyl)imide) and heated at 220 °C for 10 hours, similarly to the conditions described in our previous work. <sup>40</sup> The polycrystalline powder was recovered by centrifugation and washed with ethanol. NVPFO<sub>2</sub>-Nano was obtained by solvothermal synthesis. A stoichiometric mixture of VO(acac)<sub>2</sub> (Sigma-Aldrich), NaF (Sigma-Aldrich) and H<sub>3</sub>PO<sub>4</sub> (molar ratio of 1/1.5/1) was placed in a 100 mL Teflon Parr autoclave with a mixture 4.5 mL ethanol / 4.5 mL distilled water and heated at 180°C for 10 hours. NVPFO<sub>2</sub>-Bulk was prepared by solid-state reaction from VPO<sub>4</sub> (homemade), VOPO<sub>4</sub> (homemade), NaF (Sigma-Aldrich) and Na<sub>2</sub>CO<sub>3</sub> (Sigma-Aldrich) with a molar ratio 1:1:1:1 as described earlier. <sup>41</sup> A

mechanical grinding was first applied in order to get a homogeneous mixture, then the resulting powder was pelletized and heated under argon flow in a gold crucible at 550°C for 2 hours.  $\text{VPO}_4$  and  $\text{VOPO}_4$  were obtained from  $\alpha\text{-VOPO}_4\cdot 2\text{H}_2\text{O}$  homemade precursor. First,  $\alpha\text{-VOPO}_4\cdot 2\text{H}_2\text{O}$  was obtained by heating 5 g of  $\text{V}_2\text{O}_5$  (Sigma-Aldrich) in a mixture composed by 40 mL of phosphoric acid, 110 mL of nitric acid (Sigma-Aldrich) and 130 mL of distilled water at 100 °C during 3 hours. The resulting yellowish powder is washed by acetone. The freshly obtained  $\text{VOPO}_4\cdot 2\text{H}_2\text{O}$  was dehydrated at 250°C under  $\text{O}_2$  to produce  $\text{VOPO}_4$ . This later was then reduced under argon/hydrogen flow at 890 °C during 2 hours to synthesize  $\text{VPO}_4$ .

## 2.2 Characterization techniques

X-ray diffraction (XRD) measurements were carried out by using a BRUKER D8 ADVANCE diffractometer in  $\theta$ - $\theta$  configuration, equipped with a  $\text{Cu K}_{\alpha 1,2}$  X-ray source. The acquisition was performed in the  $2\theta$  angular range of 10° – 140° with a step size of 0.0197°. The Rietveld refinements were performed using the FullProf Suite.<sup>42</sup>

Scanning electron microscopy (SEM) images were taken without any conductive deposition by a Hitachi Model S-3400N microscope. A gold deposition was made on  $\text{NVPFO}_2$ -Bulk sample to improve the quality of the images. SEM-FEG (field emission gun) images were obtained on a Hitachi SU-70 microscope. Transmission electron microscopy (TEM) was carried out with the Tecnai spirit G2 microscope. The powder was sonicated for 20 min in ethanol before the analysis.

The chemical analysis of the Na, P and V contents was performed by inductively coupled plasma-optical emission spectroscopy (ICP-OES) using a Varian Model 720-ES spectrometer, after a complete dissolution of the powders into a concentrated hydrochloric acid (HCl) solution.

X-ray photoelectron spectroscopy (XPS) spectra were collected through Omicron Argus X-ray photoelectron spectrometer for an applied power of 280 W and a monochromated  $\text{Al-K}_{\alpha}$  radiation source (1486.6 eV). Charge correction was done by calibrating the C 1s peak at a binding energy of 284.8 eV.

Raman spectra were acquired with a confocal LabRAM HR Evolution micro-spectrometer from Horiba, using a 633-nm laser source. They were collected in the range 100-1300  $\text{cm}^{-1}$ ,

using a 10.6 mm (NA 0.5) focal length lens and with acquisition time of 20 s and 40 accumulations.

Magic Angle Spinning Nuclear Magnetic Resonance (MAS NMR) experiments were carried out using standard Bruker 2.5 mm MAS probes and a 30 kHz spinning frequency.  $^{31}\text{P}$  MAS NMR spectra were acquired on a Bruker Avance III 100 MHz spectrometer at a resonance frequency of 40.6 MHz. A Hahn echo sequence was used synchronized with one rotor period rotation, with a  $90^\circ$  pulse of  $1.1\ \mu\text{s}$  and a recycle delay of 1 s.  $\text{H}_3\text{PO}_4$  85% (Sigma-Aldrich) was used as external reference for 0 ppm chemical shift.  $^{23}\text{Na}$  MAS-NMR spectra were acquired using a Bruker Avance 500 MHz spectrometer, equipped with a 11.7 T widebore magnet (operating at Larmor frequency of 132.3 MHz for  $^{23}\text{Na}$ ). A short pulse length of  $1.1\ \mu\text{s}$  corresponding to a selective  $\pi/8$  pulse determined by using a 0.1 M NaCl aqueous solution was employed. Chemical shifts are referenced relative to an aqueous 0.1M NaCl solution at 0 ppm. The spectral width was set to 1 MHz and the recycle delay of 0.5 s, which was long enough to avoid  $T_1$  saturation effects. The baseline distortions resulted from the spectrometer dead time ( $5\text{-}10\ \mu\text{s}$ ) were removed computationally by using a polynomial baseline correction routine.

The electrical properties of  $\text{Na}_3\text{V}_2(\text{PO}_4)_2\text{FO}_2$  compounds were investigated by electrochemical impedance spectroscopy (EIS). For this purpose, the powders were pressed into pellets of 13 mm diameter applying 200 MPa by means of a uniaxial press. Prior to pressing, NVPFO<sub>2</sub>-Nano and NVPFO<sub>2</sub>-Bulk powders were mixed with camphor (about 2 wt.%) to provide enough mechanical strength allowing to extract the pellets from the die after pressing. Subsequently, the pellets were heat-treated at 250 °C for 1 h under air to evaporate the camphor. Contrary to the two others samples, NVPFO<sub>2</sub>-Iono could be well pelletized without camphor. Moreover, the evaporation of camphor at 250 °C would decompose the IL. Finally, gold electrodes were sputtered on the parallel and opposite faces of each pellet to ensure electrical contacts. EIS measurements were performed using a Solartron 1260 Impedance/Gain Phase Analyzer in the frequency range between 1 MHz and 1 Hz, with an applied root mean square voltage of 100 mV, 10 points per decade and 20 measures per point. Impedance of all the samples were measured under heating and cooling in air on a two-probe sample holder and over the temperature range of 100 - 300 °C. Among them, NVPFO<sub>2</sub>-Iono was left at 300 °C for 6h to completely remove the IL and then entered into the cooling process.

The electrochemical performances of the materials were tested in CR2032-type coin cells. The cells were assembled in an argon-filled glovebox ( $\text{H}_2\text{O}$ ,  $\text{O}_2 \leq 0.1$  ppm), with sodium metal as counter electrode. The positive electrodes were prepared as a mixture containing the active material, carbon black, and polyvinylidene fluoride (PVDF) in NMP (N-Methyl-2-pyrrolidone) with the ratio of 88/7/5 (by wt.%). After two hours of thorough mixing, the black ink was casted as a flat film by doctor blade on an aluminum foil and dried in an oven at  $80^\circ\text{C}$ . Disks were cut, then pressed under 5 tons and finally dried overnight at  $80^\circ\text{C}$  under vacuum. The electrodes have a typical active mass loading around  $4.5 - 5 \text{ mg.cm}^{-2}$ . A homemade electrolyte containing a  $1 \text{ mol.L}^{-1}$  solution of  $\text{NaPF}_6$  (Strem Chemical; 99%) in ethylene carbonate and dimethyl carbonate ( $\text{EC/DMC} = 1/1$ ) with 2 wt.% of fluoroethylene carbonate (FEC) was used for all the electrochemical tests. The assembled cells were cycled in galvanostatic mode, from C/20 to 2C cycling rates between 2.5 and 4.3 V vs.  $\text{Na}^+/\text{Na}$ . The theoretical capacity being  $130 \text{ mAh.g}^{-1}$  (corresponding to 2  $\text{Na}^+$  reversibly extracted from  $\text{NVPFO}_2$ ), the rate C/20 corresponds to the exchange of 2  $\text{Na}^+$  in 20 hours. Galvanostatic Intermittent Titration Technique (GITT) measurements were performed in half-cells versus Na after three cycles of formation at C/20. GITT measurements of  $\text{NVPFO}_2$  consisted in a series of 30 min galvanostatic charge/discharge at C/25 followed by a relaxation up to 1 mV/h between 2.5 and 4.3 V to achieve a nearly steady state.

Full cells HC //  $\text{NVPFO}_2$ -Nano were tested in CR2032-type coin cells with a mass ratio  $m(\text{NVPFO}_2)/m(\text{HC}) \approx 2.35$ . The positive electrode possesses a diameter of 16 mm ( $\sim 9 \text{ mg}$ ) whereas the negative electrode is slightly smaller (15 mm). The assembled full cells were cycled in galvanostatic mode, from C/20 to 2C cycling rates (based on  $\text{NVPFO}_2$  electrode) in a voltage range of 2.5 and 4.3 V and in the same electrolyte as described previously.

### 3 Results and discussions

#### 3.1 Structural and morphological characterization

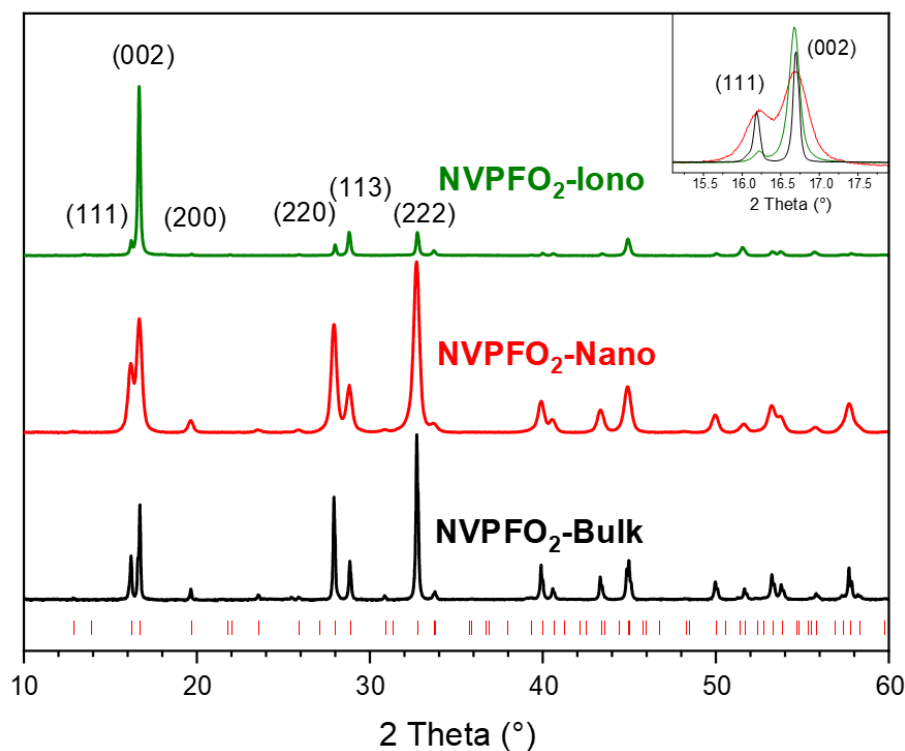


Figure 1. X-ray diffraction patterns of NVPFO<sub>2</sub>-Iono (green curve), NVPFO<sub>2</sub>-Nano (red curve) and NVPFO<sub>2</sub>-Bulk (black curve). The red ticks correspond to theoretical positions as reported in ICDD 01-083-7199. The inset shows the enlargement of (111) and (002) reflections.

The powder XRD patterns illustrated in **Figure 1** and the Rietveld refinements presented in **Figure S1** confirm that the three synthesis methods (solid-state reaction, solvothermal and ionothermal) lead to the synthesis of pure Na<sub>3</sub>V<sup>4+</sup><sub>2</sub>(PO<sub>4</sub>)<sub>2</sub>FO<sub>2</sub> (NVPFO<sub>2</sub>) phase. For each compound, all the diffraction peaks could be indexed in the space group *P4<sub>2</sub>/mnm* and the lattice parameters, reported in **Table 1**, are in good agreement with those of Na<sub>3</sub>V<sup>4+</sup><sub>2</sub>(PO<sub>4</sub>)<sub>2</sub>FO<sub>2</sub>, the end member composition of the Na<sub>3</sub>V<sup>3+</sup><sub>2-y</sub>V<sup>4+</sup><sub>y</sub>(PO<sub>4</sub>)<sub>2</sub>F<sub>3-y</sub>O<sub>y</sub> (0 ≤ y ≤ 2) solid solution.<sup>12,40,43</sup>

Table 1. Lattice parameters obtained by the Rietveld refinement of the XRD patterns, coherent domain sizes calculated using (220) and (002) reflections.

	a (Å)	c (Å)	(220) (nm)	(002) (nm)	Space group
NVPFO <sub>2</sub> -Iono	9.0098(1)	10.6278(1)	52	52	P4 <sub>2</sub> /mnm
NVPFO <sub>2</sub> -Nano	9.0214(2)	10.6216(3)	23	21	P4 <sub>2</sub> /mnm
NVPFO <sub>2</sub> -Bulk	9.0330(1)	10.6137(2)	64	70	P4 <sub>2</sub> /mnm



Additionally, ICP analyses confirm the expected cationic ratio (**Table S1**). A comparison of the X-ray diagrams (**Figure 1**) clearly shows differences in the diffraction peaks width and preferential orientation, suggesting huge variations of crystallite size and morphology within the series of NVPFO<sub>2</sub>. Indeed, compared to observations made for NVPFO<sub>2</sub>-Nano and NVPFO<sub>2</sub>-Bulk, the very intense (002) reflection observed for NVPFO<sub>2</sub>-Iono suggests an oriented particles growth in the (ab) plane leading to platelet (2D) morphology. Furthermore, the dissimilar diffraction peak broadening, highlighted in the inset of **Figure 1**, unveils disparate crystallite sizes caused by the different synthesis conditions. The coherent domains calculated using Scherrer equation are reported in **Table 1** and reveal that high temperature solid state reaction leads to the biggest crystallites (~ 70 nm) whereas the solvothermal synthesis to the smallest ones (~ 20 nm). Moreover, the similar coherent domains calculated with (002) and (220) reflections suggest an isotropic crystal growth for all synthesis routes, despite an anisotropic particles' growth by ionothermal reaction. Finally, the internal strains generated by heterogeneous and limited crystallite sizes distributed within the primary particles result in difficulties to perfectly fit the peak profile during structural refinement, which could explain the slightly different lattice parameters within the NVPFO<sub>2</sub> series (**Table 1** and **Figure S1**). Consequently, the chemical composition has to be confirmed by local environmental characterization techniques such as ss-NMR, as it will be done latter.

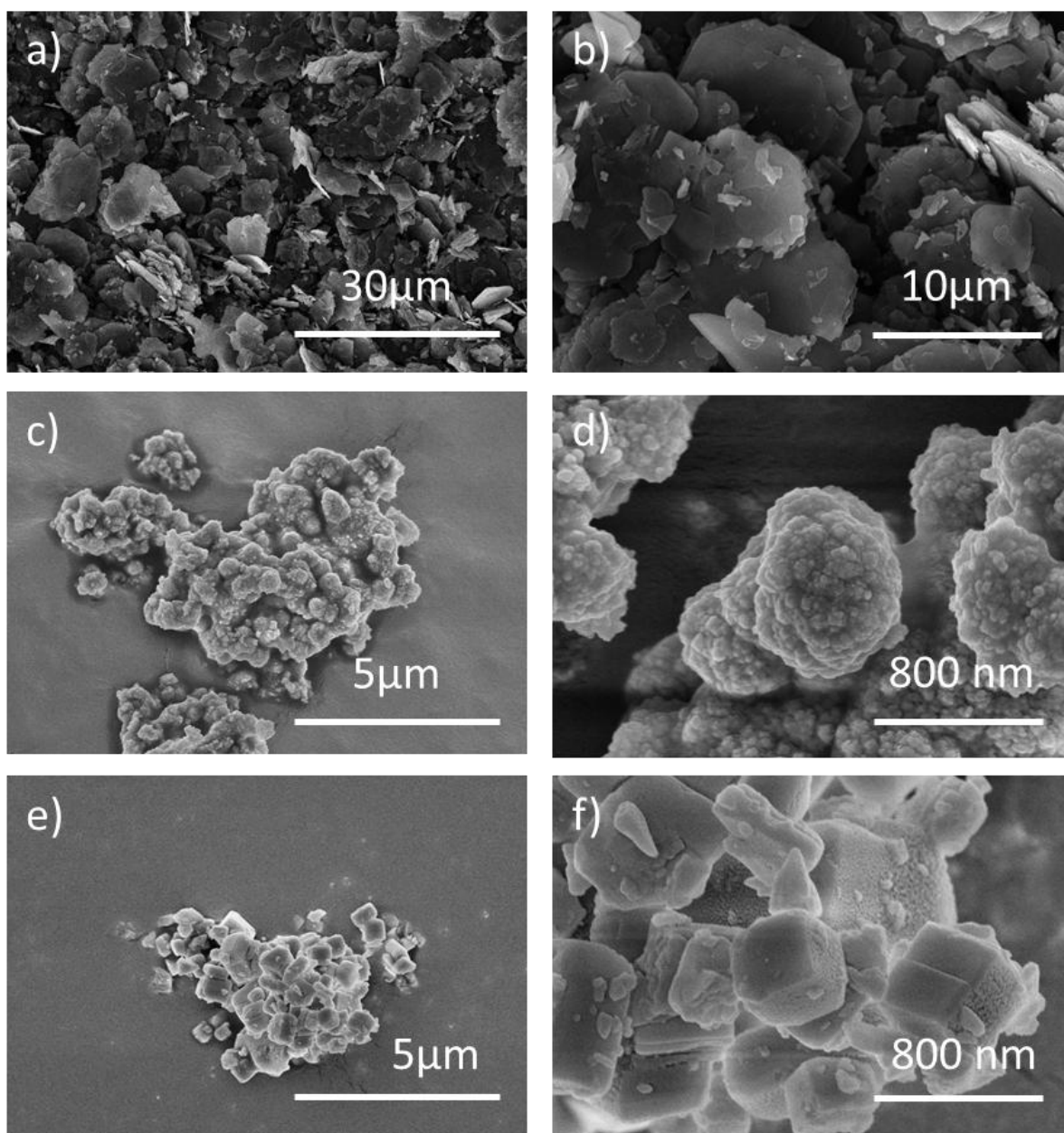


Figure 2. a), b) SEM images of NVPFO<sub>2</sub>-Iono. c), d) SEM-FEG images of NVPFO<sub>2</sub>-Nano; e), f) SEM-FEG images of NVPFO<sub>2</sub>-Bulk.

SEM, SEM-FEG (**Figure 2**) and TEM images (**Figure S2**) further confirm the various morphologies of NVPFO<sub>2</sub> materials obtained by the different syntheses methods. The NVPFO<sub>2</sub>-Iono, which is obtained by topochemical reaction from layered  $\alpha$ -VOPO<sub>4</sub>·2H<sub>2</sub>O,<sup>40</sup> is characterized by aggregated flakes with an average length around 5-10  $\mu$ m and thickness of 100-200 nm (**Figures 2 a-b and S2**). The small fragments that can be distinguished probably comes from pieces of big flakes. HRTEM analyses further revealed that the platelets exhibit (220) crystallographic planes through lattice fringes (**Figure S3 a-b**), which perfectly fits to the exalted intensity of (002) diffraction peak observed by XRD. Thus, it can be concluded that the Na<sup>+</sup> diffusion channels along the [110] and [1 $\bar{1}$ 0] directions are situated in the plane

of the flakes (**Figure S4**). NVPFO<sub>2</sub>-Nano synthesized by solvothermal process presents quite different morphology (**Figure 2c-d**). It is characterized by aggregates made of randomly agglomerated spherical secondary particles of diameter ~500 nm. These latter are constructed with smaller primary particles around 30 nm whose size is in good agreement with the crystallite size determined by XRD (**Table 1**). The different lattice fringes observed by HRTEM (**Figure S3**) for NVPFO<sub>2</sub>-Nano (0.32 nm (220), 0.53 nm (002) and 0.55 nm (111)) support the spherical morphology of the small primary particles and the absence of preferential orientation. Finally, the shape of NVPFO<sub>2</sub>-Bulk obtained by the high temperature solid-state reaction approximates to cubes varying from hundreds of nanometers to several micrometers (**Figure 2e-f**). Moreover, the thickness of NVPFO<sub>2</sub>-Bulk cubes makes the lattice fringes measurement impossible.

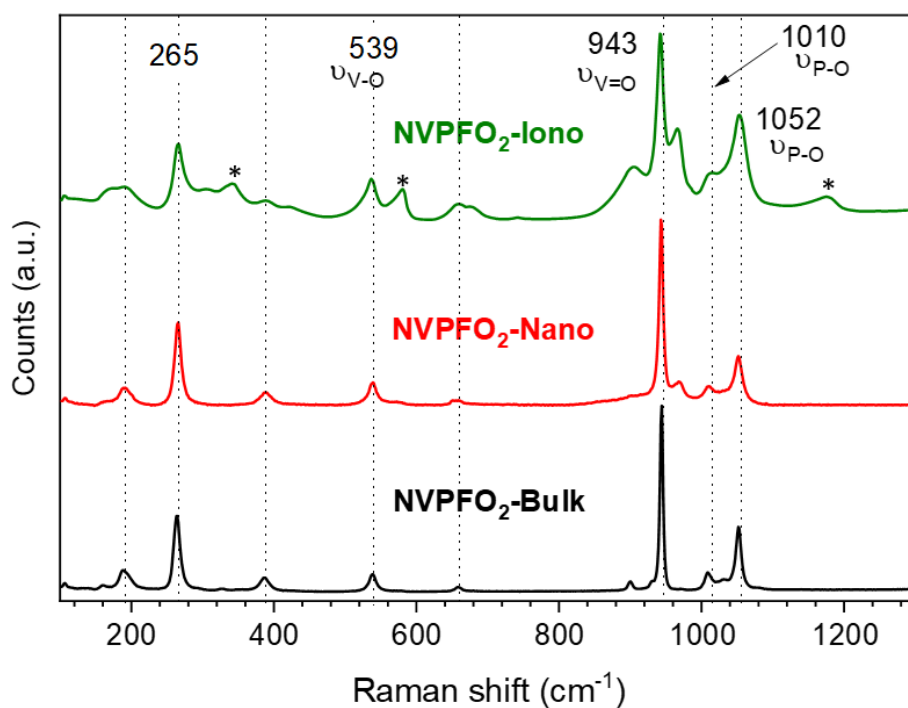


Figure 3. Raman spectra of NVPFO<sub>2</sub>-Iono (green), NVPFO<sub>2</sub>-Nano (red) and NVPFO<sub>2</sub>-Bulk (black). The band marked with a star on the Raman spectrum corresponds to EMI TFSI ionic liquid.

The series of NVPFO<sub>2</sub> was further characterized by various spectroscopic techniques to probe the Na, P and V local environments and confirm the composition deduced from Rietveld refinements. As illustrated on the Raman spectra in **Figure 3**, all materials possess the typical signature of Na<sub>3</sub>V<sub>2</sub>(PO<sub>4</sub>)FO<sub>2</sub> with peaks at 539 cm<sup>-1</sup>, 943 cm<sup>-1</sup>, 1010 cm<sup>-1</sup> and 1052 cm<sup>-1</sup> attributed to the vibrations of V-O, V=O and phosphate groups respectively.<sup>39,44,45</sup> As reported in our previous work on the topochemical reaction mechanism happening during the ionothermal synthesis of NVPFO<sub>2</sub>, the ionic liquid functionalizes the particles' surface to

create an IL coating, which can be seen as an “artificial Solid Electrolyte Interface”.<sup>40</sup> This latter, which in some cases stabilizes the electrode material upon cycling and favors ionic adsorption on the surface and/or alkaline diffusion through the material,<sup>46–48</sup> is observed on NVPFO<sub>2</sub>-Iono spectrum (**Figure 3**) and on HRTEM images (**Figure S5**). Indeed, the band marked with a star on the Raman spectrum are in rather good agreement with those expected for the EMI TFSI ionic liquid.<sup>49–52</sup> IL can also be detected on the surface of NVPFO<sub>2</sub>-Iono through XPS analysis that reveals the presence of N 1s and S 2p peaks originated from imidazolium ring and TFSI respectively (as shown by the surveys in the energy range of 0 – 1100 eV in **Figure S6** and by the quantification given in **Table S2**). Meanwhile, the F 1s spectra (**Figure 4a**) clearly show a signal at 684.1 eV for all the compounds, corresponding to the fluorine in the polyanionic materials whereas NVPFO<sub>2</sub>-Iono presents a second peak at 688.6 eV, which is the agreement with the presence of CF<sub>3</sub> from EMI TFSI.<sup>47,53,54</sup> However, this IL coating does not seem to affect the inorganic core phase. The V 2p XPS spectra of the NVPFO<sub>2</sub> series are presented in **Figure 4b** and the spectrum of each compound exhibits two broad peaks at 517.3 eV and 524.8 eV corresponding to the V 2p<sub>3/2</sub> and V 2p<sub>1/2</sub> transitions. These binding energies are consistent with the expected ones for this polyanionic material with V<sup>4+</sup> environment and demonstrate for NVPFO<sub>2</sub>-Iono that the IL coating does not affect the electronic structure of vanadium present near the surface.<sup>55</sup>

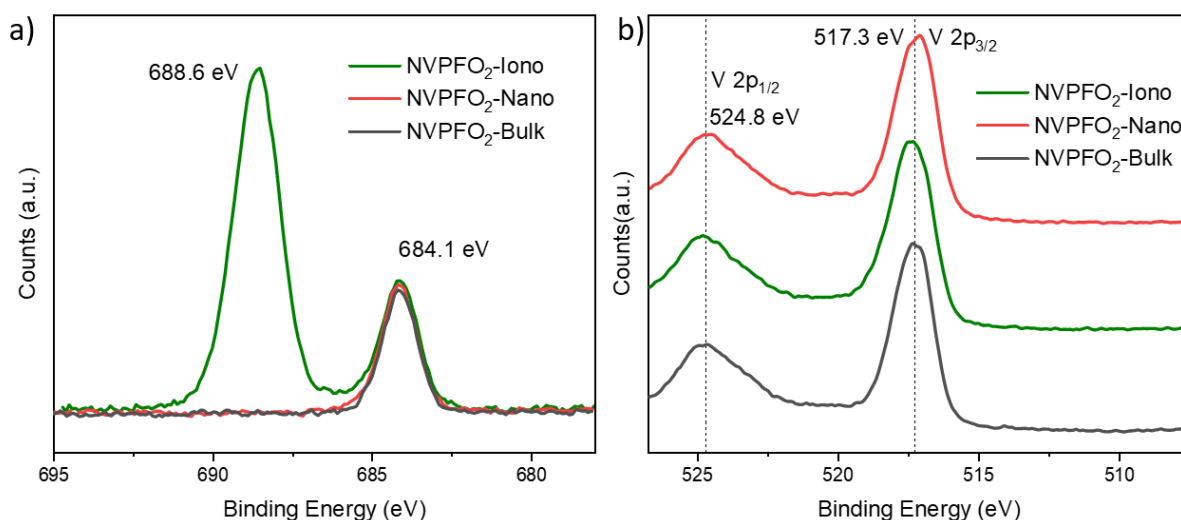


Figure 4. a) F 1s XPS spectra and b) V 2p XPS spectra for all the NVPFO<sub>2</sub> materials.

For all compounds, the <sup>23</sup>Na ss-NMR spectrum (**Figure 5a**) reveals a main peak at ~77 ppm, whose position is mainly due to the hyperfine interaction between the Na<sup>+</sup> nucleus and the unpaired electron of paramagnetic V<sup>4+</sup> ions and is characteristic of Na(OV<sup>4+</sup>)<sub>2</sub> environment.<sup>12,56</sup> The absence of signals at higher isotropic shift confirms the absence of V<sup>3+</sup>

in these phases and validates the  $\text{Na}_3\text{V}^{4+}_2(\text{PO}_4)\text{FO}_2$  composition.<sup>14,36,41,56</sup> Meanwhile, the broader signal for NVPFO<sub>2</sub>-Nano could be the consequence of disorder due to particle's downsizing.<sup>34</sup> <sup>31</sup>P ss-NMR spectra obtained for all NVPFO<sub>2</sub> show very intense signal at ~ 0 ppm corresponding to P(OV<sup>4+</sup>)<sub>4</sub> local environment (**Figure 5b**).<sup>56</sup> Once again the absence of signal induced by Fermi contact shift at ~ 1500, 3000 ppm, 4500 ppm or 6000 ppm as previously observed for the  $\text{Na}_3\text{V}_2(\text{PO}_4)(\text{F},\text{O})_2$  series excludes the existence of V<sup>3+</sup> in the compounds.<sup>22,56</sup> The enlarged area in **figure 5c** unfolds more details on the signal located around 0 ppm. Three distinct signals are observed for NVPFO<sub>2</sub>-Bulk that most probably correspond to the inequivalent local environments for the phosphorus. On the other hand, the signals of NVPFO<sub>2</sub>-Nano and NVPFO<sub>2</sub>-Iono are broader, asymmetric and less resolved due to the small changes on the local environment brought by the nanosizing / specific morphology.<sup>57</sup> Therefore, the use of different synthesis methods allows to obtain  $\text{Na}_3\text{V}^{4+}_2(\text{PO}_4)\text{FO}_2$  materials with extremely different particles size, with and without coating, offering thus an ideal series to study the downsizing and IL coating effects on the transport properties and energy storage performance.

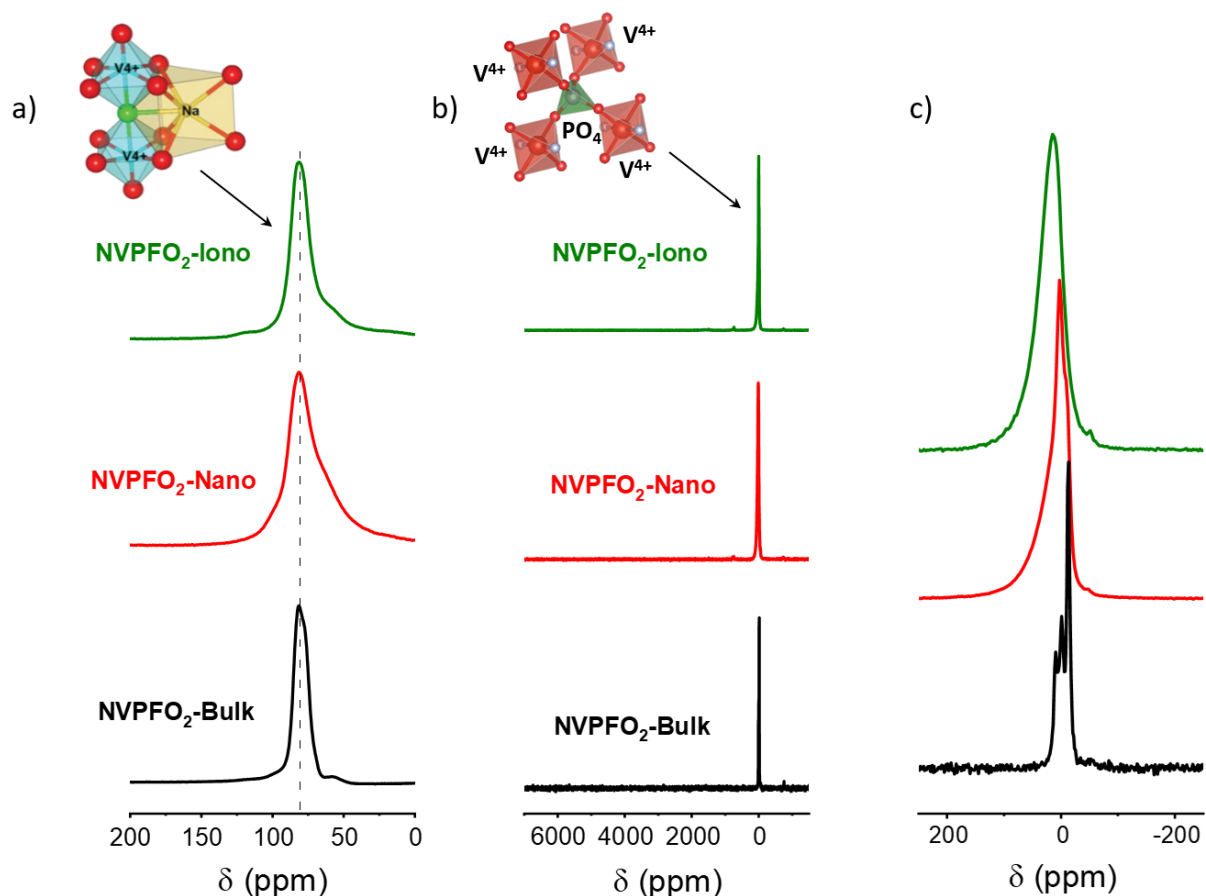


Figure 5. a)  $^{23}\text{Na}$  solid-state MAS NMR spectra of NVPFO<sub>2</sub>-Iono (green), NVPFO<sub>2</sub>-Nano (red) and NVPFO<sub>2</sub>-Bulk (black); b) corresponding  $^{31}\text{P}$  solid-state MAS NMR spectra and c) the enlargement of the signals around 0 ppm.

### 3.2 Transport kinetics and energy storage performance

The energy storage performance of the three Na<sub>3</sub>V<sub>2</sub>(PO<sub>4</sub>)<sub>2</sub>FO<sub>2</sub> samples were first evaluated by cyclic voltammetry and galvanostatic measurements in half-cell configuration. The electrode formulation (88 wt.% active material / 7 wt.% carbon black / 5 wt.% PVDF) and the mass loading of ~5 mg/cm<sup>2</sup> are expected to emphasize on the influence of the different NVPFO<sub>2</sub> electrode materials. **Figure 6a-c** shows the galvanostatic charge-discharge curves obtained within the potential window 2.5 - 4.3V vs Na<sup>+</sup>/Na at different current intensities, whereas the reversible capacity evolution depending on the C-rate is represented in **Figure 6d**. All electrode materials exhibit two reversible plateaus or pseudo-plateaus at around 3.6 and 4 V vs Na<sup>+</sup>/Na, attributed to the V<sup>5+</sup>/V<sup>4+</sup> redox couple that is activated by reversible Na<sup>+</sup> extraction and in perfect agreement with the values reported in the literature.<sup>12,58</sup> Sharma et al. reported that the reaction mechanisms upon charge and discharge are composed of first order transitions (two-phase transition) separated by second order ones (solid solution).<sup>59</sup> At C/20, NVPFO<sub>2</sub>-Nano and NVPFO<sub>2</sub>-Iono exhibit similar reversible high capacities (~115 mAh.g<sup>-1</sup>

and  $\sim 110 \text{ mAh.g}^{-1}$  respectively), close to the theoretical one ( $130 \text{ mAh.g}^{-1}$ ). However, NVPFO<sub>2</sub>-Nano possesses a much better capacity retention when the charge rate increases up to 2C. Meanwhile, the discharge capacity of NVPFO<sub>2</sub>-Bulk already merely reaches  $67 \text{ mAh.g}^{-1}$  at C/20 and quickly drops when the current becomes higher. The full initial capacity recovering after several cycles of fast charge/discharge clearly shows that the difference in performance mainly originates from the kinetics limitations specific to the electrode material.

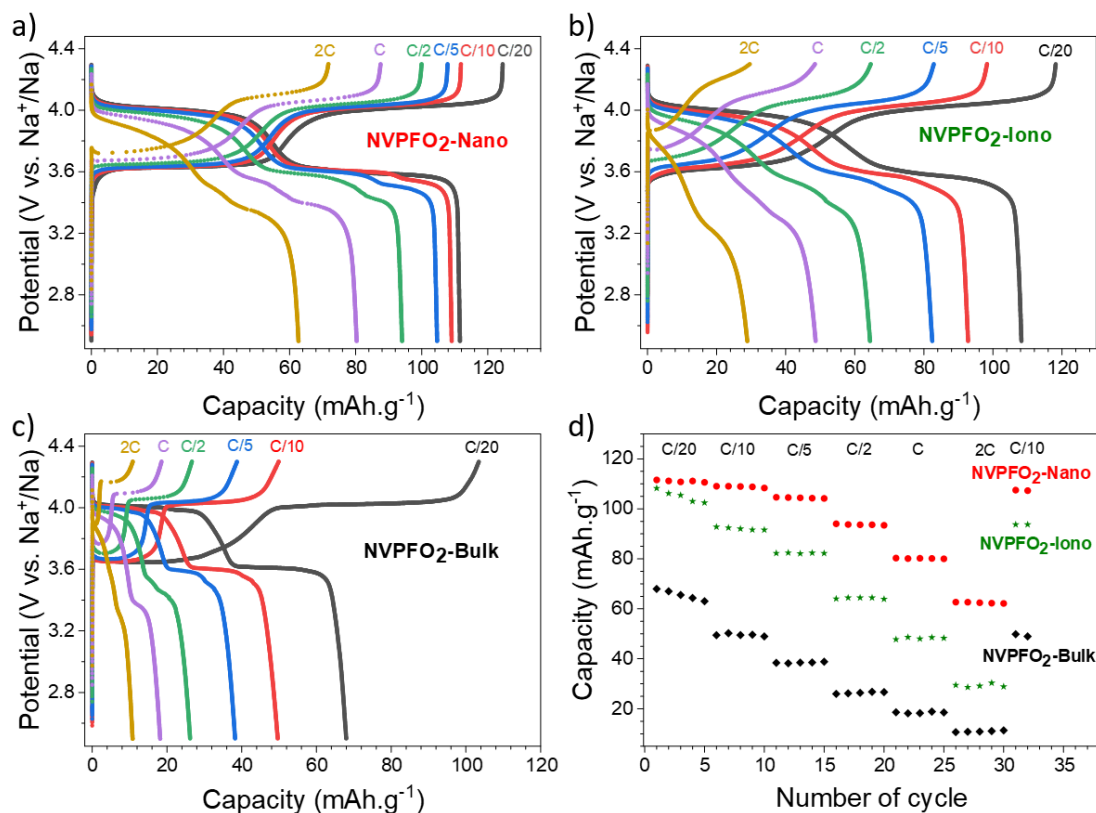


Figure 6. a)-c) Charge and discharge curves of all the NVPFO<sub>2</sub> materials at different cycling rates and d) rate capabilities obtained for all these materials, from C/20 to 2C.



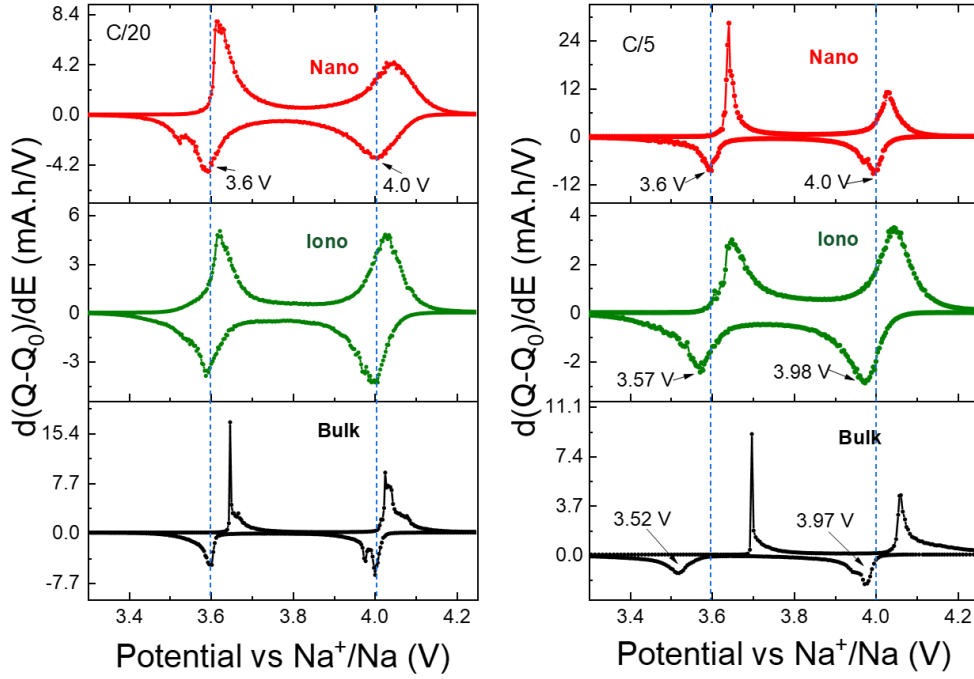


Figure 7. First derivative curves of the second cycle of galvanostatic charge/discharge process of all the NVPFO<sub>2</sub> materials at C-rates of C/20 and C/5.

This is supported by the evolution of the polarization when the charge rate increases as illustrated in **Figure 7** that shows the first derivative curves of the 2<sup>nd</sup> galvanostatic cycle (**Figure 6**) performed at C/20 and C/5.

At C/20, the average discharge redox potentials for all electrode materials are observed at 4 V and 3.6 V vs Na<sup>+</sup>/Na. These potentials remain unchanged for NVPFO<sub>2</sub>-Nano when the charge rate increases to C/5, whereas the values drop to 3.98 V and 3.57 V for NVPFO<sub>2</sub>-Iono and 3.97 V and 3.52 V for NVPFO<sub>2</sub>-Bulk. Similarly, the  $\Delta E_p$  (potential difference between charge/discharge) increases for NVPFO<sub>2</sub>-Iono and more significantly for NVPFO<sub>2</sub>-Bulk, which leads to a system with slower kinetics, lower average discharge potential and thus, lower energy density. This clearly shows that the resistance R (sum of electrical and ionic resistance) follows the trend  $R_{\text{Bulk}} > R_{\text{Iono}} > R_{\text{Nano}}$  and thus, strongly depends on the active material as it is the only variable parameter in this electrode series. Therefore, the transport properties were further investigated to get a deeper insight into the influence of the particles' size and IL coating.

The complex impedance data of all the NVPFO<sub>2</sub> compounds reveal quite distinct electrical behaviors. **Figure 8** depicts complex impedance plots of each NVPFO<sub>2</sub> sample recorded at 200 °C under heating, and also upon cooling for NVPFO<sub>2</sub>-Iono. Here, the complex impedance data ( $Z^*$ ) have already been normalized regarding the shape factor ( $l/A$ , thickness over area)



of each sample, according to the relation  $Z_s^* = Z^* \cdot A/l$  given rise to the specific impedance ( $Z_s^*$ ). This approach allows a straight comparison between the impedance response of samples. For samples NVPFO<sub>2</sub>-Nano (**Figure 8a**) and NVPFO<sub>2</sub>-Bulk (**Figure 8b**), the overall electrical resistivity can be promptly read at the low-frequency intercept of the impedance data with the real part of the specific impedance ( $Z_s'$ ). Thus, sample NVPFO<sub>2</sub>-Bulk is about one order of magnitude more resistive than sample NVPFO<sub>2</sub>-Nano. Indeed, sample NVPFO<sub>2</sub>-Bulk is so resistive that its overall impedance is out of the equipment impedance range at this temperature, explaining thus the dispersion of impedance data at low-frequency range. A common feature between the electrical behavior of these samples is the distorted semi-circles probably caused by a jointly contribution of grains and grain boundaries at high and middle-frequency ranges, respectively.<sup>39</sup> On contrast, NVPFO<sub>2</sub>-Iono (**Figure 8c**) presents an impedance response completely different from that of the other samples and even less resistive than that of the sample NVPFO<sub>2</sub>-Nano. Its impedance response combines a high-frequency semicircle probably linked to the ionic transport enhanced by the IL coating and a low-frequency highly depressed semicircle due to electrode polarization phenomenon. In theory, if the ionic liquid is rigidly attached on the surface of NVPFO<sub>2</sub> particles and only Na<sup>+</sup> ions are mobile, a steep increase of the imaginary part of the impedance should take place in low-frequency range.<sup>47</sup> Since this is not the case, we hypothesized that the ionic molecular species that constitute the ionic liquid could be also relatively mobile either because they are not grafted or because of the high temperature employed for the impedance spectroscopy measurements. In any case, the dependence of the real part of permittivity on frequency reveals a logarithmic increase of the relative permittivity in low-frequency range typical of an ion blocking effect, precluding the hypotheses of a majority electronic contribution to the overall charge transport (**Figure S7**). Therefore, the electrical resistivity related to the Na<sup>+</sup> transport can be roughly read at the middle frequency real part projection of the specific impedance ( $Z_s'$ ) between the two semicircles. Furthermore, once this sample is heated up to 300 °C and then cooled down, its electrical behavior changes entirely (**Figure 8d**) due to the degradation of the IL whereas the electrical conductivity is nearly the same upon heating and cooling for the two other electrode materials (**Figure 9**). In this case, the final electrical behavior of the NVPFO<sub>2</sub>-Iono is much alike that of the NVPFO<sub>2</sub>-Bulk, highly resistive and with two impedance contributions likely coming from grains and grain boundaries contributions. The polarization phenomenon caused by the grain boundaries and the ion blocking effect can be visualized respectively as a middle-frequency pseudo plateau and low-frequency logarithmic increase of the real part of permittivity (**Figure S7**).

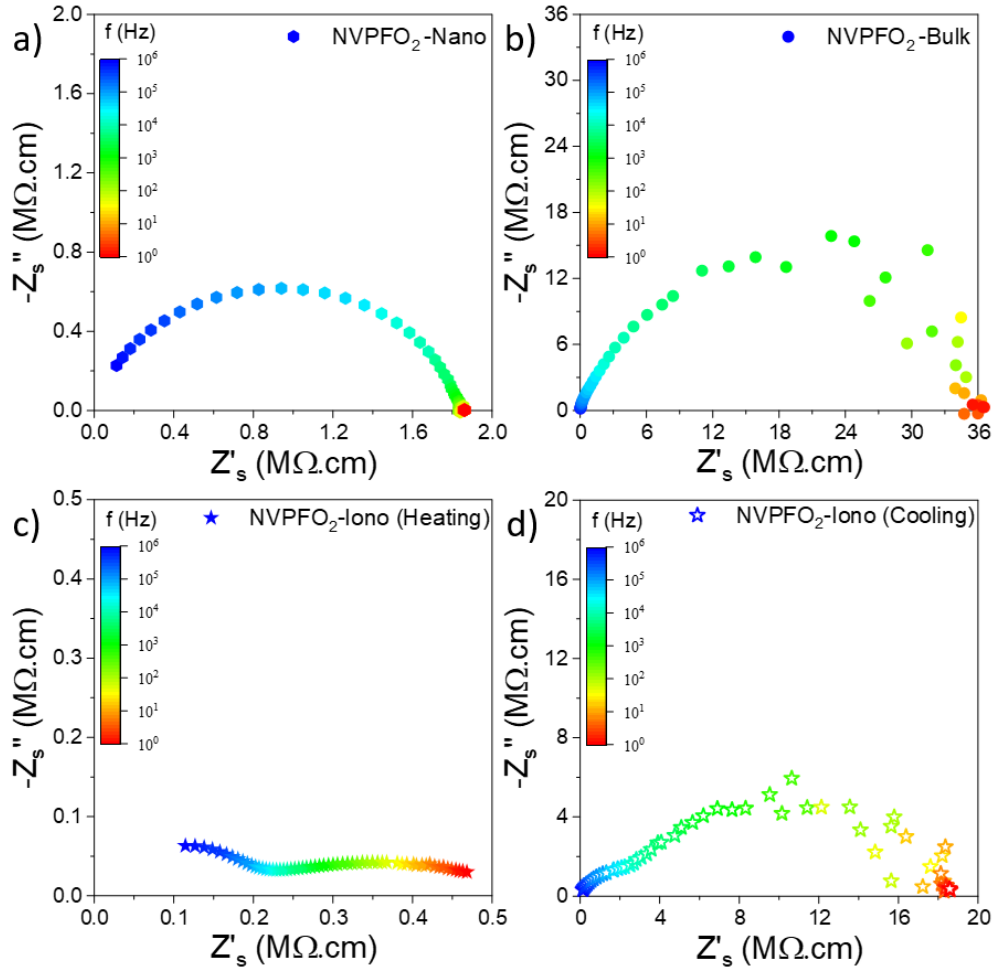


Figure 8. EIS analyses of  $\text{Na}_3\text{V}_2(\text{PO}_4)_2\text{F}_{0.2}$  samples recorded at  $200^\circ\text{C}$  under heating for NVPFO<sub>2</sub>-Nano a) and NVPFO<sub>2</sub>-Bulk b) as well as for NVPFO<sub>2</sub>-Iono under heating (c) and under cooling (d). The complex impedance data shown here have already been normalized regarding the shape factor of each sample for comparison purposes.

The dependence of the overall electrical conductivity on the inverse of temperature is plotted by applying the linearized form of the Arrhenius-like relation (Eq. 1), which is mostly used for ionic conductors but sometimes also applied for electronic conductors.<sup>60–62</sup>

$$\sigma T = \sigma_0 \exp\left(\frac{-E_a}{k_B T}\right) \quad (1)$$

Here,  $\sigma_0$  is the pre-exponential factor,  $E_a$  is the activation energy for ionic conductivity,  $k_B$  is the Boltzmann constant, and  $T$  is the absolute temperature. Following this methodology, the linear fit slope is proportional to the activation energy, which therefore provides access to the energetic barrier of the mechanism responsible for the electrical transport.<sup>62</sup> **Figure 9** exhibits the Arrhenius-like plots of the overall electrical conductivity of the NVPFO<sub>2</sub> compounds synthesized under different conditions. Overall, the dependence of the electrical conductivity on temperature for NVPFO<sub>2</sub>-Nano seems to present a low ( $T < 180^\circ\text{C}$ ) and a high ( $T >$

180 °C) temperature regimes, due to the dominating electronic transport at low temperatures and the mixed ionic-electronic conducting behavior at higher temperatures.<sup>39</sup> The activation energy of the high temperature regime is considerably higher than the low-temperature one (**Figure 9**). Two activation energy regimes have been also visualized for the micrometric NVPFO<sub>1</sub> compounds reported in literature by Broux et al.<sup>63</sup> Nevertheless, in that case the transition takes place around the temperature of 130 °C and was attributed to a structural change. Besides, in the low temperature regime, this micrometric NVPFO<sub>1</sub> compound (obtained by solid-state synthesis) shows much lower conductivity and higher activation energy than the NVPFO<sub>2</sub>-Nano studied in this work (**Figure 9**). For example, the conductivity and activation energy for the NVPFO<sub>1</sub> reference are  $\sim 10^{-10} \text{ S}\cdot\text{cm}^{-1}$  and 0.86 eV at 95 °C, while they are  $3 \times 10^{-8} \text{ S}\cdot\text{cm}^{-1}$  and 0.43 eV for NVPFO<sub>2</sub>-Nano at 100 °C.<sup>63</sup> Likewise, NVPFO<sub>2</sub>-Bulk in this study also presents electrical conductivity much lower and activation energy higher than the NVPFO<sub>2</sub>-Nano compound. Thus, this result demonstrates the strong enhancement of electronic conductivity induced by particles downsizing.

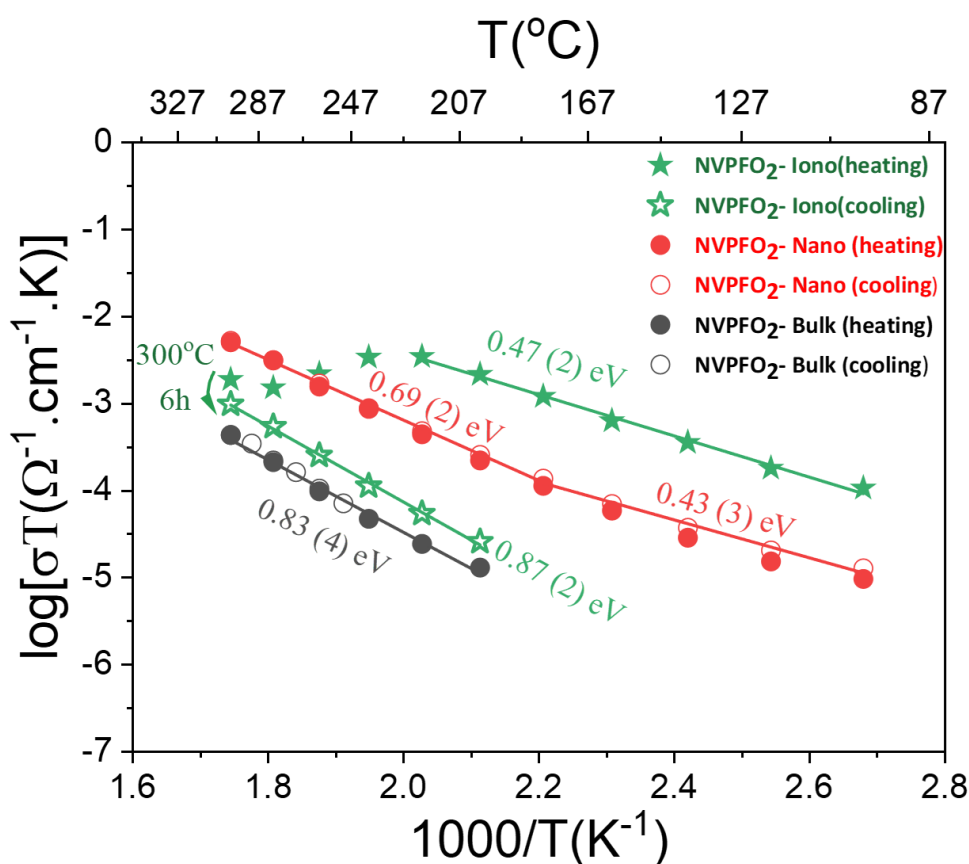


Figure 9. Arrhenius-like plots of the dependence of the overall electric conductivity on the inverse temperature for NVPFO<sub>2</sub> samples synthesized in different conditions.

On the other hand, the sample coated with the IL shows at low temperatures an overall conductivity even higher than the nanometric NVPFO<sub>2</sub> ( $2.7 \times 10^{-7} \text{ S}\cdot\text{cm}^{-1}$  vs  $3 \times 10^{-8} \text{ S}\cdot\text{cm}^{-1}$

<sup>1</sup> at 100 °C) and a similar activation energy within errors of ~0.45 eV. However, above 220 °C the conductivity drops considerably probably due to the IL decomposition. After six hours at 300 °C, the conductivity of the sample gradually decreases upon cooling to values two orders of magnitude smaller than those observed upon heating (**Figure 9**). The activation energy is almost the double than that observed under heating, suggesting a totally different conduction mechanism. Meanwhile, the electrical conductivity of NVPFO<sub>2</sub>-Iono under cooling is in the same order of magnitude of that observed for NVPFO<sub>2</sub>-Bulk with similar activation energies of ~0.85 eV, which indicates the strong ionic conductivity improvement brought by IL coating. Barpanda et al. have demonstrated a lithium conductivity enhancement by IL grafting on lithium fluoride sulfate compounds,<sup>47</sup> thus in our case Na<sup>+</sup> conductivity in NVPFO<sub>2</sub>-Iono would be strongly improved.

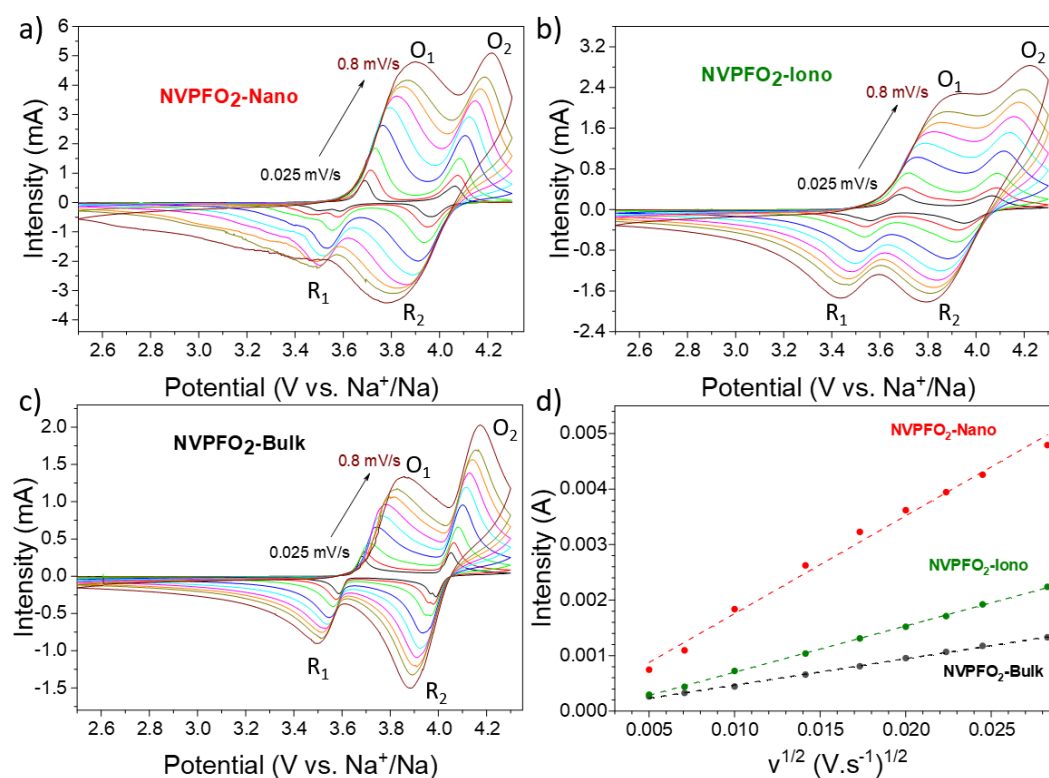


Figure 10. CV curves at different scan rates and the corresponding linear fitting curves between the maximum current (*i<sub>p</sub>*) and the square root of the scan rate ( $v^{1/2}$ ) for the O<sub>1</sub> peak of each compound.

The Na<sup>+</sup> diffusion during redox reactions was investigated through the CV analysis at various scan rates from 0.25 mV/s to 0.8 mV/s in the potential range between 2.5 V and 4.3 V vs Na<sup>+</sup>/Na to avoid possible electrolyte degradation (**Figure 10a-c**). Two oxidation and two reduction peaks, representing respectively the two plateaus in galvanostatic charge and

discharge curves, are observed for all the NVPFO<sub>2</sub> materials. Interestingly, at high scan rates the two oxidation and reduction peaks strongly overlap for NVPFO<sub>2</sub>-Iono, which suggests the absence of Na<sup>+</sup> ordering and a single-phase reaction mechanism. This could be explained by the enhanced Na<sup>+</sup> conductivity determined by impedance spectroscopy. Furthermore, the overlap is globally less pronounced for NVPFO<sub>2</sub>-Nano and even less for NVPFO<sub>2</sub>-Bulk, which for instance exhibits two well-defined reduction peaks for all scan rate ranges. **Figure 10d** and **Figure S8** depict the evolution of the peak current intensity (*i<sub>p</sub>*) versus the square root of the scan rate (*v*<sup>1/2</sup>) that allows to estimate Na<sup>+</sup> diffusion coefficients using Randles-Sevcik equation (**Supplementary part S8 and Table 2**).

*Table 2. Diffusion coefficients calculated from CV curves using for Randles-Sevcik equation.*

D (cm <sup>2</sup> s <sup>-1</sup> )	NVPFO <sub>2</sub> -Nano	NVPFO <sub>2</sub> -Iono	NVPFO <sub>2</sub> -Bulk
O <sub>2</sub>	4.06x10 <sup>-11</sup>	1.32x10 <sup>-11</sup>	5.73x10 <sup>-12</sup>
O <sub>1</sub>	3.28x10 <sup>-11</sup>	7.67x10 <sup>-12</sup>	2.43x10 <sup>-12</sup>
R <sub>2</sub>	1.78x10 <sup>-11</sup>	5.16x10 <sup>-12</sup>	3.10x10 <sup>-12</sup>
R <sub>1</sub>	1.73x10 <sup>-11</sup>	4.66x10 <sup>-12</sup>	1.08x10 <sup>-12</sup>

Nanospherical NVPFO<sub>2</sub>-Nano reveals the best diffusion capability with a 4.06×10<sup>-11</sup> cm<sup>2</sup>.s<sup>-1</sup> at the O<sub>2</sub> oxidation peak, nearly one order of magnitude higher than the cubic NVPFO<sub>2</sub>-Bulk with a calculated diffusion coefficient of 5.73×10<sup>-12</sup> cm<sup>2</sup>.s<sup>-1</sup>. Quite surprisingly, the IL coated NVPFO<sub>2</sub> exhibits only intermediate diffusion coefficient during redox reactions (e.g. 1.32×10<sup>-11</sup> cm<sup>2</sup>.s<sup>-1</sup> for the higher potential Na<sup>+</sup> extraction) whereas a high ionic mobility had been measured by impedance spectroscopy. It is thus possible that the ionic liquid coating only enhances the Na<sup>+</sup> mobility on the surface of the electrode material and at grain boundaries. During electrochemical impedance spectroscopy measurements, NaTFSI can be formed at the surface of NVPFO<sub>2</sub>-Iono while the cationic part of the ionic liquid attached on NVPFO<sub>2</sub> surface transfers its charge to inorganic material.<sup>64</sup> Thus, the measured conductivity would be that of Na<sup>+</sup> in the IL coating. On the other hand, this coating does not affect the Na<sup>+</sup> diffusion in the bulk of the NVPFO<sub>2</sub> material. Thus, Na<sup>+</sup> diffusion during oxidation/reduction (CV or galvanostatic charge/discharge) is still limited by the solid-state diffusion within bulk NVPFO<sub>2</sub>. Na<sup>+</sup> extraction or insertion necessary involves an electron transfer to compensate the charge (vanadium oxidation or reduction) and as the electronic conductivity of micrometric NVPFO<sub>2</sub> is very low, this limits the intercalation/extraction processes and thus Na<sup>+</sup> diffusion. Besides, GITT measurements confirm this trend as detailed in Supplementary Parts S8-S9.

According to the **Figure 11a**, all the positive electrode materials reveal good reversible capacity retentions after 80 cycles at C/5. Overall, all NVPFO<sub>2</sub> possess stable capacity retention showing that particles' downsizing and IL coating does not lead to electrode degradation or irreversible reaction that can be detrimental to practical application. On the other hand, the coulombic efficiency of NVPFO<sub>2</sub>-Bulk is not stable (**Figure 11b**). Starting from the 20<sup>th</sup> cycle, the positive electrode suffers frequent coulombic efficiency loss that might be due to the electrolyte degradation, electric noise or the contact problem in the coin cell. However, its worse electrochemical performance than NVPFO<sub>2</sub>-Iono and NVPFO<sub>2</sub>-Nano at this charge and discharge rate emphasizes the benefits of nanosizing and surface coating.

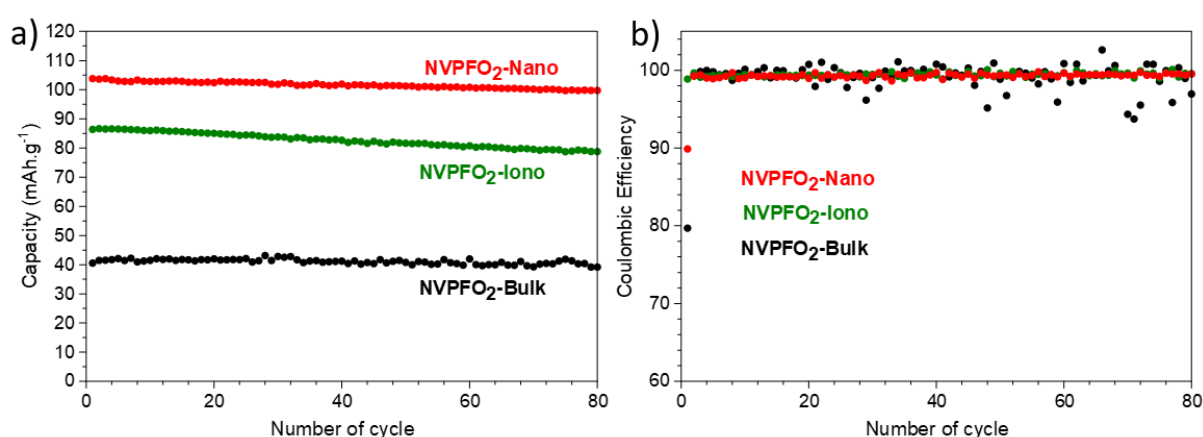


Figure 11. a) Evolution of reversible capacity upon long term cycling at C/5 and b) related coulombic efficiency of all the NVPFO<sub>2</sub> materials.

Bearing in mind the very promising performance obtained for nanospherical NVPFO<sub>2</sub>, a full cell NVPFO<sub>2</sub>-Nano versus hard carbon was assembled and tested. Considering the electrode composition (88% active material / 7% C / 5% PVDF), the full cell shows excellent performance with energy density of 320 Wh.kg<sup>-1</sup> at C/20 and 310 Wh.kg<sup>-1</sup> at C/10 (**Figure 12a**). For comparison, Iarchuk et al. reported the same energy density for NVPFO<sub>2</sub> but with electrode loadings containing only 70 % of active material.<sup>65</sup> Moreover, the full cell still exhibits 70% of its initial capacity at 1C (**Figure 12b**). The Ragone plot given in **Figure 12c** demonstrates the variation of energy density along with the increase of power density. Compared to a recent study reported by Notten et al., NVPFO<sub>2</sub>-Nano displays similar high-rate performance in full cell than an optimized carbon-coated NVPF,<sup>17</sup> which validates the extremely promising performance of our electrode nano-material. Meanwhile, the long cycling stability of full cell needs further optimisation as the capacity retention remains limited around 70% after 56 cycles (**Figure S11**). A better balancing between positive and

negative electrode mass and other optimisations such as electrolyte formulation would allow to improve the long-term capacity retention.

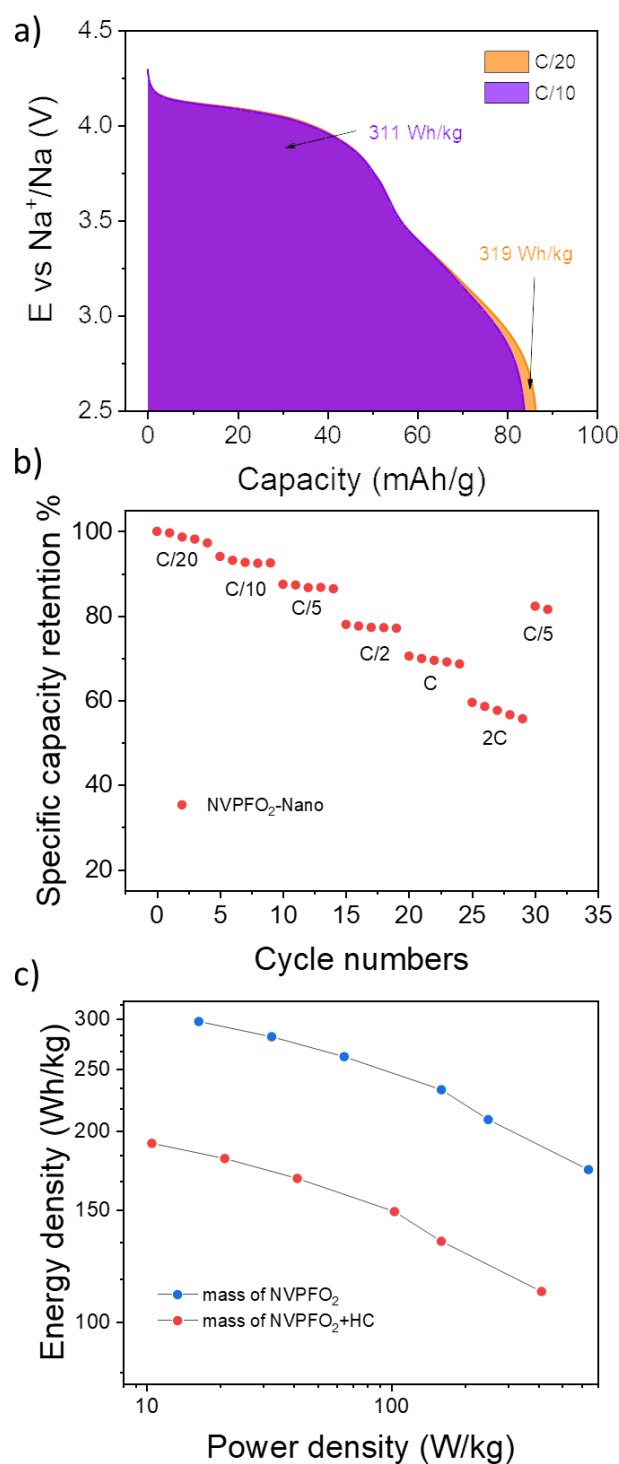


Figure 12. a) Energy density calculated for NVPFO<sub>2</sub>-Nano at C/20 and C/10, b) specific capacity retention in % upon increasing C-rate and c) Ragone plots of the NVPFO<sub>2</sub>-Nano full cell, the blue points correspond to the capacity calculated based on NVPFO<sub>2</sub> mass and the red points on both electrode mass.

## 4. Conclusion

In summary, NVPFO<sub>2</sub> electrode materials were synthesized through three different synthesis methods leading to a series of NVPFO<sub>2</sub> with different characteristics, which allows investigating separately particles' size impact and the effect of an IL coating on the electronic conductivity, diffusion capacity of Na<sup>+</sup> and the energy storage performance. A set of spectroscopic characterizations (NMR, XPS and Raman) confirms the Na<sub>3</sub>V<sub>2</sub>(PO<sub>4</sub>)<sub>2</sub>FO<sub>2</sub> composition for each compound and reveals that the ionic liquid coating on NVPFO<sub>2</sub>-Iono does not affect the vanadium nor the sodium local environment. Impedance spectroscopy measurements demonstrate that particle's downsizing improves the electronic conductivity by more than two orders of magnitude in the low temperature range whereas the IL coating strongly enhances the ionic mobility. For instance, NVPFO<sub>2</sub>-Nano and NVPFO<sub>2</sub>-Iono present electrical conductivities around  $3 \times 10^{-8} \text{ S} \cdot \text{cm}^{-1}$  and  $2.5 \times 10^{-7} \text{ S} \cdot \text{cm}^{-1}$  at 100°C whereas the one of NVPFO<sub>2</sub>-Bulk is estimated below  $10^{-10} \text{ S} \cdot \text{cm}^{-1}$ . The broad and overlapping redox peaks on CV curves for NVPFO<sub>2</sub>-Iono, in addition to the slopping profile on GCD curves, suggest the absence of Na<sup>+</sup> ordering during cycling which may be due to the enhanced ionic mobility brought by the IL coating. Moreover, when NVPFO<sub>2</sub>-Iono loses its IL coating upon thermal degradation, the conductivity and activation energy become similar to NVPFO<sub>2</sub>-Bulk, which confirms the beneficial role of IL coating. Concerning energy storage performance, NVPFO<sub>2</sub>-Nano demonstrates the best rate capacity retention confirming that a good electronic conductivity of positive electrode materials is primordial for high rate cycling, and its absence cannot be fully compensated by improving the ionic diffusion. Besides NVPFO<sub>2</sub>-Nano performance in full cell are very promising considering the absence of carbon-coating nor formulation optimization. Finally, it was shown that particles downsizing strongly increases the electronic conductivity whereas an ionic liquid coating enhances the ionic mobility, thus the next step would be to combined both approach to develop a more performant electrode material.

## Author contributions

The manuscript was written by J.O, R.F, R.B.N., S.C and L.C. through support of all the co-authors. The study was conceptualized by J.O, S.C. and L.C. The synthesis of the different materials were done by R.F. J.O and C.B.; R.B.N. performed all the electrochemical impedance spectroscopy measurements and analyzed the data; C.P. prepared all the electrode



as well as the half and full cells; D.C. performed ss-NMR acquisitions and did data interpretation. Raman measurements and interpretation were done by J.O.

## **Conflicts of interest**

The authors declare no conflicts of interest.

## **Acknowledgement**

The authors thank the Materials Physics and Chemistry Doctoral School (ED397) of Sorbonne University for the funding of Runhe FANG's PhD thesis, as well as the financial support of Région Nouvelle Aquitaine, of the French National Research Agency (STORE-EX Labex Project ANR-10-LABX-76-01 and the Project Nano-INSPIRE ANR-21-CE50-0006) and of the European Union's Horizon 2020 research and innovation program under grant agreement No 875629 (NAIMA project). The authors also thank Emmanuel PETIT, Cathy DENAGE, Eric LEBRAUD (ICMCB) for their technical support.

## 5. Reference

- 1 IPCC Working Group I, *Climate Change 2021: The Physical Science Basis*, 2021.
- 2 Y. Hu, S. Komaba, M. Forsyth, C. Johnson and T. Rojo, *Small Methods*, 2019, **3**, 1900184.
- 3 I. Hasa, S. Mariyappan, D. Saurel, P. Adelhelm, A. Y. Kuposov, C. Masquelier, L. Croguennec and M. Casas-Cabanas, *J. Power Sources*, 2021, **482**, 228872.
- 4 J.-M. Tarascon, *Joule*, 2020, **4**, 1616–1620.
- 5 K. M. Abraham, *ACS Energy Lett.*, 2020, 3544–3547.
- 6 J.-N. Chotard, G. Rousse, R. David, O. Mentré, M. Courty and C. Masquelier, *Chem. Mater.*, 2015, **27**, 5982–5987.
- 7 C. V. Manohar, A. Raj K, M. Kar, M. Forsyth, D. R. MacFarlane and S. Mitra, *Sustain. Energy Fuels*, 2018, **2**, 566–576.
- 8 W. Zhou, L. Xue, X. Lü, H. Gao, Y. Li, S. Xin, G. Fu, Z. Cui, Y. Zhu and J. B. Goodenough, *Nano Lett.*, 2016, **16**, 7836–7841.
- 9 F. Chen, V. M. Kovrugin, R. David, O. Mentré, F. Fauth, J.-N. Chotard and C. Masquelier, *Small Methods*, 2019, **3**, 1800218.
- 10 S. Park, J. N. Chotard, D. Carlier, I. Moog, M. Courty, M. Duttine, F. Fauth, A. Iadecola, L. Croguennec and C. Masquelier, *Chem. Mater.*, 2021, **33**, 5355–5367.
- 11 C. Xu, J. Zhao, E. Wang, X. Liu, X. Shen, X. Rong, Q. Zheng, G. Ren, N. Zhang, X. Liu, X. Guo, C. Yang, H. Liu, B. Zhong and Y. Hu, *Adv. Energy Mater.*, 2021, **11**, 2100729.
- 12 L. H. B. Nguyen, T. Broux, P. S. Camacho, D. Denux, L. Bourgeois, S. Belin, A. Iadecola, F. Fauth, D. Carlier, J. Olchowka, C. Masquelier and L. Croguennec, *Energy Storage Mater.*, 2019, **20**, 324–334.
- 13 M. Bianchini, F. Fauth, N. Brisset, F. Weill, E. Suard, C. Masquelier and L. Croguennec, *Chem. Mater.*, 2015, **27**, 3009–3020.

- 14 Y.-U. Park, D.-H. Seo, H. Kim, J. Kim, S. Lee, B. Kim and K. Kang, *Adv. Funct. Mater.*, 2014, **24**, 4603–4614.
- 15 Y. Qi, L. Mu, J. Zhao, Y. Hu, H. Liu and S. Dai, *Angew. Chemie Int. Ed.*, 2015, **54**, 9911–9916.
- 16 L. Zhu, H. Wang, D. Sun, Y. Tang and H. Wang, *J. Mater. Chem. A*, 2020, **8**, 21387–21407.
- 17 K. Chayambuka, M. Jiang, G. Mulder, D. L. Danilov and P. H. L. Notten, *Electrochim. Acta*, 2022, **404**, 139726.
- 18 N. Eshraghi, S. Caes, A. Mahmoud, R. Cloots, B. Vertruyen and F. Boschini, *Electrochim. Acta*, 2017, **228**, 319–324.
- 19 F. Li, Y. Zhao, L. Xia, Z. Yang, J. Wei and Z. Zhou, *J. Mater. Chem. A*, 2020, **8**, 12391–12397.
- 20 L. Zhu, Q. Zhang, D. Sun, Q. Wang, N. Weng, Y. Tang and H. Wang, *Mater. Chem. Front.*, 2020, **4**, 2932–2942.
- 21 T. Broux, F. Fauth, N. Hall, Y. Chatillon, M. Bianchini, T. Bamine, J. Leriche, E. Suard, D. Carlier, Y. Reynier, L. Simonin, C. Masquelier and L. Croguennec, *Small Methods*, 2019, **3**, 1800215.
- 22 J. Olchowka, L. H. B. Nguyen, T. Broux, P. Sanz Camacho, E. Petit, F. Fauth, D. Carlier, C. Masquelier and L. Croguennec, *Chem. Commun.*, 2019, **55**, 11719–11722.
- 23 A. Criado, P. Lavela, C. Pérez-Vicente, G. F. Ortiz and J. L. Tirado, *J. Electroanal. Chem.*, 2020, **856**, 113694.
- 24 M. Wang, K. Wang, X. Huang, T. Zhou, H. Xie and Y. Ren, *Ceram. Int.*, 2020, **2**, 1–9.
- 25 C. Guo, J. Yang, Z. Cui, S. Qi, Q. Peng, W. Sun, L.-P. Lv, Y. Xu, Y. Wang and S. Chen, *J. Energy Chem.*, 2022, **65**, 514–523.
- 26 I. L. Matts, S. Dacek, T. K. Pietrzak, R. Malik and G. Ceder, *Chem. Mater.*, 2015, **27**, 6008–6015.

- 27 Y. Zhang, S. Guo and H. Xu, *J. Mater. Chem. A*, 2018, **6**, 4525–4534.
- 28 L. H. B. Nguyen, J. Olchowka, S. Belin, P. Sanz Camacho, M. Duttine, A. Iadecola, F. Fauth, D. Carlier, C. Masquelier and L. Croguennec, *ACS Appl. Mater. Interfaces*, 2019, **11**, 38808–38818.
- 29 C. Shen, H. Long, G. Wang, W. Lu, L. Shao and K. Xie, *J. Mater. Chem. A*, 2018, **6**, 6007–6014.
- 30 J. Xun, Y. Zhang and H. Xu, *Inorg. Chem. Commun.*, 2020, **115**, 107884.
- 31 J. Zhao, L. Mu, Y. Qi, Y. S. Hu, H. Liu and S. Dai, *Chem. Commun.*, 2015, **51**, 7160–7163.
- 32 A. Mukherjee, T. Sharabani, R. Sharma, S. Okashy and M. Noked, *Batter. Supercaps*, 2020, **3**, 510–518.
- 33 Y. Qi, L. Mu, J. Zhao, Y.-S. Hu, H. Liu and S. Dai, *J. Mater. Chem. A*, 2016, **4**, 7178–7184.
- 34 R. Fang, J. Olchowka, C. Pablos, P. S. Camacho, D. Carlier, L. Croguennec and S. Cassaignon, *Batter. Supercaps*, 2022, **5**, e202100179.
- 35 Y. Qi, J. Zhao, C. Yang, H. Liu and Y.-S. Hu, *Small Methods*, 2019, **3**, 1800111.
- 36 P. Serras, V. Palomares, J. Alonso, N. Sharma, J. M. López del Amo, P. Kubiak, M. L. Fdez-Gubieda and T. Rojo, *Chem. Mater.*, 2013, **25**, 4917–4925.
- 37 P. R. Kumar, K. Kubota, Y. Miura, M. Ohara, K. Gotoh and S. Komaba, *J. Power Sources*, 2021, **493**, 229676.
- 38 D. Semykina, O. Podgornova and N. Kosova, *Mater. Today Proc.*, 2020, **25**, 497–500.
- 39 R. Fang, J. Olchowka, C. Pablos, R. Bianchini Nuernberg, L. Croguennec and S. Cassaignon, *ACS Appl. Energy Mater.*, 2022, **5**, 1065–1075.
- 40 J. Olchowka, L. H. B. Nguyen, E. Petit, P. S. Camacho, C. Masquelier, D. Carlier and L. Croguennec, *Inorg. Chem.*, 2020, **59**, 17282–17290.
- 41 T. Broux, T. Bamine, F. Fauth, L. Simonelli, W. Olszewski, C. Marini, M. Ménétrier,

- D. Carlier, C. Masquelier and L. Croguennec, *Chem. Mater.*, 2016, **28**, 7683–7692.
- 42 J. Rodríguez-Carvajal, *Phys. B Condens. Matter*, 1993, **192**, 55–69.
- 43 N. Sharma, P. Serras, V. Palomares, H. E. A. Brand, J. Alonso, P. Kubiak, M. L. Fdez-Gubieda and T. Rojo, *Chem. Mater.*, 2014, **26**, 3391–3402.
- 44 F. D. Hardcastle and I. E. Wachs, *J. Phys. Chem.*, 1991, **95**, 5031–5041.
- 45 C. J. Antony, A. Aatiq, C. Y. Panicker, M. J. Bushiri, H. T. Varghese and T. K. Manojkumar, *Spectrochim. Acta - Part A Mol. Biomol. Spectrosc.*, 2011, **78**, 415–419.
- 46 J. Olchowka, R. Invernizzi, A. Lemoine, J. Allouche, I. Baraille, D. Flahaut and L. Guerlou-Demourgues, *J. Electrochem. Soc.*, 2020, **167**, 100527.
- 47 P. Barpanda, R. Dedryvère, M. Deschamps, C. Delacourt, M. Reynaud, A. Yamada and J.-M. Tarascon, *J. Solid State Electrochem.*, 2012, **16**, 1743–1751.
- 48 J. Olchowka, T. Tailliez, L. Bourgeois, M. A. Dourges and L. Guerlou-Demourgues, *Nanoscale Adv.*, 2019, **1**, 2240–2249.
- 49 R. Baddour-Hadjean and J. P. Pereira-Ramos, *Chem. Rev.*, 2010, **110**, 1278–1319.
- 50 A. Criado, P. Lavela, G. Ortiz, J. L. Tirado, C. Pérez-Vicente, N. Bahrou and Z. Edfouf, *Electrochim. Acta*, 2020, **332**, 135502.
- 51 Y. Cai, X. Cao, Z. Luo, G. Fang, F. Liu, J. Zhou, A. Pan and S. Liang, *Adv. Sci.*, 2018, **2**, 1800680.
- 52 K. Fujii, T. Fujimori, T. Takamuku, R. Kanzaki, Y. Umebayashi and S. I. Ishiguro, *J. Phys. Chem. B*, 2006, **110**, 8179–8183.
- 53 C. J. Jafta, X. G. Sun, H. Lyu, H. Chen, B. P. Thapaliya, W. T. Heller, M. J. Cuneo, R. T. Mayes, M. P. Paranthaman, S. Dai and C. A. Bridges, *Adv. Funct. Mater.*, 2021, **31**, 2008708.
- 54 T. Sugimoto, M. Kikuta, E. Ishiko, M. Kono and M. Ishikawa, *J. Power Sources*, 2008, **183**, 436–440.
- 55 Z. Tong, Y. Qi, J. Zhao, L. Liu, X. Shen and H. Liu, *Waste and Biomass Valorization*,

- 2020, **11**, 2201–2209.
- 56 L. H. B. Nguyen, P. Sanz Camacho, T. Broux, J. Olchowka, C. Masquelier, L. Croguennec and D. Carlier, *Chem. Mater.*, 2019, **31**, 9759–9768.
- 57 W. Papawassiliou, J. P. Carvalho, N. Panopoulos, Y. Al Wahedi, V. K. S. Wadi, X. Lu, K. Polychronopoulou, J. B. Lee, S. Lee, C. Y. Kim, H. J. Kim, M. Katsiotis, V. Tzitzios, M. Karagianni, M. Fardis, G. Papavassiliou and A. J. Pell, *Nat. Commun.*, 2021, **12**, 1–11.
- 58 L. H. B. Nguyen, A. Iadecola, S. Belin, J. Olchowka, C. Masquelier, D. Carlier and L. Croguennec, *J. Phys. Chem. C*, 2020, **124**, 23511–23522.
- 59 N. Sharma, P. Serras, V. Palomares, H. E. A. Brand, J. Alonso, P. Kubiak, M. L. Fdez-Gubieda and T. Rojo, *Chem. Mater.*, 2014, **26**, 3391–3402.
- 60 J.-L. Souquet, in *Encyclopedia of Glass Science, Technology, History, and Culture*, Wiley, 2021, pp. 453–463.
- 61 M. C. Ungureanu, M. Lévy and J. L. Souquet, *Ionics (Kiel)*, 1998, **4**, 200–206.
- 62 R. B. Nuernberg, *Ionics (Kiel)*, 2020, **26**, 2405–2412.
- 63 T. Broux, B. Fleutot, R. David, A. Brüll, P. Veber, F. Fauth, M. Courty, L. Croguennec and C. Masquelier, *Chem. Mater.*, 2018, **30**, 358–365.
- 64 A. Paoletta, G. Bertoni, W. Zhu, D. Campanella, A. La Monaca, G. Girard, H. Demers, A. C. Gheorghe Nita, Z. Feng, A. Vijh, A. Guerfi, M. Trudeau, M. Armand and S. A. Krachkovskiy, *J. Am. Chem. Soc.*, 2022, **5**, jacs.1c11466.
- 65 A. R. Iarchuk, D. V. Sheptyakov and A. M. Abakumov, *ACS Appl. Energy Mater.*, 2021, **4**, 5007–5014.